



**HAL**  
open science

## Probing the origins of magnetism in 2 at% Fe-implanted 4H-SiC

Leifeng Zhang, Lindor Diallo, Abdeslem Fnidiki, Luc Lechevallier, Alain Declémy, Williams Lefebvre, Jean Juraszek

► **To cite this version:**

Leifeng Zhang, Lindor Diallo, Abdeslem Fnidiki, Luc Lechevallier, Alain Declémy, et al.. Probing the origins of magnetism in 2 at% Fe-implanted 4H-SiC. Scripta Materialia, 2020, 188, pp.157-163. 10.1016/j.scriptamat.2020.07.030 . hal-02922644

**HAL Id: hal-02922644**

**<https://normandie-univ.hal.science/hal-02922644>**

Submitted on 22 Aug 2022

**HAL** is a multi-disciplinary open access archive for the deposit and dissemination of scientific research documents, whether they are published or not. The documents may come from teaching and research institutions in France or abroad, or from public or private research centers.

L'archive ouverte pluridisciplinaire **HAL**, est destinée au dépôt et à la diffusion de documents scientifiques de niveau recherche, publiés ou non, émanant des établissements d'enseignement et de recherche français ou étrangers, des laboratoires publics ou privés.



Distributed under a Creative Commons Attribution - NonCommercial 4.0 International License



23 In recent years, many efforts have been devoted to introduce 3d Transition Metals (TMs,  
24 such as Cr, Mn, Co and Fe) in semiconductors in order to fabricate DMSs [1]. DMSs allow  
25 manipulating the spin degree and the charge degree of the electrons separately and  
26 simultaneously through the electrical and magnetic fields in one material. These DMSs should  
27 possess both considerable ferromagnetic properties at room temperature and relatively high  
28 Curie temperature for industrial application. In practice, the realization of room-temperature  
29 DMS is quite challenging. Although considerable explorations have been paid to some  
30 semiconductors and oxides, like GaN-, Si-, GaAs-, ZnO- and TiO<sub>2</sub>- based [1-6], no room-  
31 temperature DMS has been successfully produced.

32 Much attention was also focused on some wide-bandgap semiconductors. SiC, with a wide  
33 bandgap (3.3 eV for 4H-SiC and 3.0 eV for 6H-SiC), high electrical breakdown field and high  
34 thermal conductivity, is used for high-temperature and high-power electronics [7]. Ab-initio  
35 calculations have predicted that doping SiC with TMs could result in a ferromagnetic ordering  
36 [8]. This phenomenon has been experimentally confirmed; ferromagnetic ordering appears at  
37 Curie Temperatures of 50, 250 and 270 K in Ni, Mn and Fe-implanted 6H-SiC [9]. High  
38 Curie Temperatures were also achieved in other TM-doped SiC semiconductors [10-14].

39 However, the origins of the magnetic effects were not clear. The magnetic components  
40 could derive from defects [15, 16], defect-TM complexes [13, 17] or presence of second-  
41 phase particles [11, 18]. With the TM impurities beyond the solubility limit, spinodal  
42 nanodecomposition as well as nanoprecipitation may occur in a range of semiconductor  
43 compounds [3]. Among those, according to recent research, the second-phase particles could  
44 probably induce the ferromagnetism for Fe-doped SiC. In SiC matrix, the Fe reaction with  
45 SiC at high temperature may induce the formation of binary Fe-silicides and ternary Fe-  
46 silicocarbides [10, 11, 13, 19, 20], some of which were reported to be magnetic. Due to the

47 presence of Fe<sub>3</sub>Si nanoparticles detected by APT in 6 at.% Fe-implanted 6H-SiC sample, a 67%  
48 ferromagnetic component was obtained from CEMS spectra [11].

49 In order to achieve an in-depth understanding of the implantation induced magnetism, we  
50 tried to produce a 2 at.% Fe-implanted 4H-SiC DMS and performed careful analyses on the  
51 microstructure by advanced characterization techniques. The relationship between Fe  
52 distribution and its contribution on the magnetism was then explored from a quantitative view.

53 Commercial near (0001)-oriented p-type 4H-SiC substrates (provided by CREE, Durham,  
54 NC, USA), with a 200 nm thickness uppermost epitaxial layer of p-type ( $n_A-n_D \sim 10^{20} \text{ cm}^{-3}$ ),  
55 were co-implanted with 30-160 keV <sup>56</sup>Fe and <sup>57</sup>Fe ions. The integrated dose can reach  $10^{16}$   
56 ions/cm<sup>2</sup>, which induces a plateau of 2 at.% Fe concentration at a depth of 20-100 nm beneath  
57 the sample surface according to the SRIM calculation [21] or experimental confirmation by  
58 Rutherford backscattering spectroscopy [22, 23]. During ion implantation, the sample was  
59 held at 550 °C in order to avoid amorphization [22]. A rapid thermal annealing was then  
60 performed at 1300 °C for 4 min to promote defect annihilation [24].

61 The microstructure was examined by APT and (S)TEM. APT technique, based on field  
62 evaporation [25], offers extensive capabilities for both 3D imaging and local chemical  
63 analyses. Specimens for APT were prepared through the lift-out methods using a dual beam  
64 SEM/FIB instrument (Zeiss Nvision 40). To conserve the region of interest (20-100 nm  
65 beneath the surface), the Fe-implanted 4H-SiC sample was capped with 500-1000 nm of Pt.  
66 Here, a Laser Assisted Wide Angle Tomographic Atom Probe (LAWATAP) was used to  
67 perform the analysis, with a practical temperature of 80 K, a detection flux of 0.003-0.004  
68 ions/s/cm<sup>2</sup> and a pulse repetition rate of 100 kHz. The wavelength of femtosecond laser pulse  
69 is 343 nm. The GPM 3D software (From GPM lab, v. 6.4) was used to do the relevant data  
70 reconstruction. The chemical compositions of the core nanoparticles were measured using the

71 iso-position cluster identification method [25]. (S)TEM was performed using a JEOL ARM-  
72 200F instrument operated at 200 kV. Selected Area Electron Diffraction Patterns (SAEDPs)  
73 and High Resolution TEM (HRTEM) images were taken to identify the crystal structures of  
74 these nanoparticles. The structural information is collected from the Crystallography Open  
75 Datasets and displayed by VESTA software [26].

76  $^{57}\text{Fe}$  CEMS technique was used at 300 K to analyze the near surface region of the irradiated  
77 sample since it has a penetration depth of about 80-100 nm [27, 28]. The spectra were  
78 measured in normal incidence using a (He-5%  $\text{CH}_4$ ) gas flow proportional counter [29] and a  
79  $\sim 1.5$  GBq radioactive source of  $^{57}\text{Co}$  in Rh matrix in constant acceleration mode. The CEMS  
80 spectra were fitted by using the four components of the Gunnlaugsson model [30] and a Fs  
81 (ferro) component. The single  $\text{Fe}_i$  (C) and  $\text{Fe}_i$  (Si) lines are attributed to the interstitial sites of  
82 Fe atoms surrounded by four C or Si atoms, respectively. The Fs (para) component  
83 corresponds to the positioning of the substitutional Fe atoms in C or Si sites. The Fd fraction  
84 is assigned to Fe atoms located in strongly disturbed zones. Besides the four components, the  
85 Fs (ferro) component was used for the Fe atoms contained in the nanoparticles and the Fe  
86 atoms diluted in the matrix for the ferromagnetic contribution. By differentiating  
87 quantitatively paramagnetism and ferromagnetism,  $^{57}\text{Fe}$  CEMS is very useful for interpreting  
88 the magnetization data measured by a MPMS 5XL SQUID magnetometer at 300 K and 10 K.

89 Here, STEM and APT were used to investigate the microstructure, and fine magnetic  
90 characterizations were performed by CEMS and SQUID. The magnetic nanoparticles were  
91 then correlated to the magnetism.

92 Fig. 1(a)-(c) exhibit massive nanoparticles from 3 different APT samples.

93 *Fig. 1*

94 These observed particles have a diameter of 1-8 nm. The calculated Fe/Si ratio for those  
95 with a minimum number of 60 atoms in core particle was plotted in Fig. 1(d). These  
96 nanoparticles correspond to a chain of Fe-silicides, including Fe<sub>2</sub>Si, Fe<sub>5</sub>Si<sub>3</sub>, Fe<sub>3</sub>Si<sub>2</sub>, FeSi and  
97 FeSi<sub>2</sub>, among which some with a higher Fe/Si ratio (or higher Fe concentration) may grow to  
98 a larger size. Notably, some C atoms were also observed in the core of particles, as exhibited  
99 in Fig. 1(e). In fact, the Fe, Si and C concentration values in these nanoparticles depend on the  
100 atomic or molecular trajectory and the subsequent 3D reconstruction. SiC has a higher  
101 evaporation field than nanoparticles, which may lead to a trajectory aberration due to the local  
102 magnification effect [25]. Other phenomena, including the molecular ion evaporation [31] and  
103 the multiple events [31, 32] may also blur the C projection trajectory, making its identification  
104 more complex in SiC. It remains a question that whether these nanoparticles behave as  
105 nanoclusters containing C atoms or nanoparticles without C atoms inside.

106 The crystal structures of nanoparticles were thus explored by (S)TEM analyses. From the  
107 HRTEM image in Fig. 2(a), one particle embedded in matrix can be distinguished. This  
108 nanoparticle exhibits lattice coherency with matrix. As seen in the Fast Fourier Transform  
109 (FFT) images of the nanoparticle (in Fig. 2(b)) and matrix (in Fig. 2(c)), there is a small  
110 lattice misfit along the horizontal direction. This is also clear in the local magnification map  
111 in Fig. 2(d). 4H-SiC phase (space group: P 6<sub>3</sub> m c) possesses hexagonal close-packed  
112 symmetry, in which “4” refers to the atomic layers in a repeat unit along the stacking direction  
113 and H represents the crystal symmetry. The interplanar distances of {0116} and {1000}  
114 planes are 0.142 nm and 0.267 nm, respectively. In the nanoparticle, the cubic Fe<sub>3</sub>Si phase  
115 (space group: F m  $\bar{3}$  m) is evidenced by two vertical lattice parameters, 0.140 nm and 0.250  
116 nm, corresponding to the inter-planar distances of {400} and {021} planes, respectively. It is  
117 inferred that the {400} plane of Fe<sub>3</sub>Si phase is oriented with {0116} plane of 4H-SiC matrix.

118

*Fig. 2*

119 The hexagonal Fe<sub>2</sub>Si phase (space group:  $\bar{P} 3 m 1$ ) could be identified from Fig. 2(e) and (f),  
120 which reveal the SAEDPs along two distinct orientations (not the exact zone axes). The  
121 extracted lattice parameters, with the values in the range 0.2018-0.2028 nm, correspond to the  
122 theoretical lattice parameter of  $\{2\bar{1}10\}$  planes (with a value of 0.2026 nm) of Fe<sub>2</sub>Si phase. The  
123 SAEDPs for the nanoparticles can only be recorded from some fields of view aligned with  
124 specific orientations, requiring tentative rotation operations. In Fig. 2(g), some ring traces  
125 were observed from the SAEDP image and the corresponding interplanar distances were  
126 measured. After comparison with all the possible lattice parameters among all Fe-silicides,  
127 Fe<sub>5</sub>Si<sub>3</sub> phase (space group:  $P 6_3 m c m$ ) could be unambiguously identified.

128 Thus, the presence of several Fe-silicides was confirmed. The repeated lattice cells for  
129 cubic Fe<sub>3</sub>Si phase, hexagonal Fe<sub>2</sub>Si phase and hexagonal Fe<sub>5</sub>Si<sub>3</sub> phase are plotted in Fig. 2(h)-  
130 (j). Since these Fe-silicides exhibit their predicted crystal structures, it is very unlikely that a  
131 significant proportion of C atoms are present in these particles. It is hence inferred that the  
132 detected C atoms in the nanoparticles should come from APT artefacts.

133 These nanoparticles formed during thermal annealing display simultaneously a size and a  
134 composition gradient along implantation depth. In Fig. 3(a), the phase of these nanoparticles  
135 evolves from Fe-rich type (Fe<sub>2</sub>Si) to Si-rich type (FeSi<sub>2</sub>) within an implantation depth 20-100  
136 nm, along with the size decrease. These observations are consistent with the Fe distribution.  
137 Based on the calculation shown in Fig. 3(b), Fe concentration peaks at a penetration depth of  
138 20-45 nm, corresponding to the presence of most Fe<sub>2</sub>Si-type nanoparticles. Due to limited  
139 reconstruction volume in APT, no Fe<sub>3</sub>Si-type nanoparticle was observed in this sample. TEM  
140 photograph in Fig. 3(c) reveals a 1-9 nm size-gradient distribution of nanoparticles beneath  
141 the implantation surface, which perfectly agrees with APT analyses. These nanoparticles

142 show various shapes (regular and irregular). This may partly explain why the Chemical  
143 Composition Correction (CCC) model [33] fails to correct the particle composition, since this  
144 model is adapted to cubic or spherical nanoparticles.

145 *Fig. 3*

146 At high temperature, a variety of stable and metastable phases appear in the binary Fe-Si  
147 phase diagram [34]. A stronger Fe-Si affinity promotes the preferential formation of Fe-  
148 silicides rather than carbides. The formation of Fe<sub>3</sub>Si could be ascribed to its high standard  
149 formation enthalpy of -94.1 kJ/mol [35], in comparison to that of 25.2 kJ/mol for Fe<sub>3</sub>C [35].  
150 Here, the possibility that ternary Fe-silicocarbides (including Fe<sub>65</sub>Si<sub>25</sub>C<sub>10</sub>, Fe<sub>70</sub>Si<sub>10</sub>C<sub>20</sub>,  
151 Fe<sub>70</sub>Si<sub>15</sub>C<sub>15</sub>, reported in [20]) are formed could be excluded, because these compounds are in  
152 an amorphous condition at above 1000 °C. For instance, Fe<sub>65</sub>Si<sub>25</sub>C<sub>10</sub> will decompose above  
153 737 K [20].

154 Moreover, the Fe concentration at the SiC interface determines the types of the Fe-silicides.  
155 Fe concentration decreases monotonously within the implantation depth 20-100 nm. The Fe  
156 diffusion is motivated by the vacancies produced during ion implantation. The high vacancy  
157 concentration near the surface region results in a corresponding high Fe concentration, since  
158 the vacancies prefer to stay closer to the free surface [36]. As measured from Fig. 3(b), the  
159 average Fe concentration is  $2.5 \pm 0.2$  at.% at a depth range 16-45 nm, and thus Fe<sub>2</sub>Si-type  
160 nanoparticles were formed. In accordance with the decreasing Fe concentration, a chain of Fe-  
161 silicides were observed.

162 Fig. 4(a) plots the CEMS spectra obtained at ambient temperature for the as-annealed  
163 sample. The spectra were fitted with 2 paramagnetic components (Fe<sub>i</sub> (C) and Fs (para)) of the  
164 Gunnlaugsson model and one ferromagnetic component (Fs (ferro)). Another 2 components,  
165 Fe<sub>i</sub> (Si) and Fd, were neglected since the samples were annealed at 1300°C [35]. The analyses

166 reveal that Fe atoms distribute in different environments. The ferromagnetic spectrum  
 167 originates from the ferromagnetic ordering of Fe. The hyperfine field distribution in Fig. 4(b)  
 168 reveals an about 32% contribution of ferromagnetic component. The ordered Fe<sub>3</sub>Si phase was  
 169 frequently reported in the literature because of its ferromagnetic contribution [11, 37-39]. The  
 170 low intensity at two intensity peaks (typically 20T and 30T [11]) suggests a low volume  
 171 fraction of ordered Fe<sub>3</sub>Si phase. This well agrees with the fact that a few Fe<sub>3</sub>Si-type  
 172 nanoparticles were observed from APT and TEM analyses. Indeed, the Fs (ferro) component  
 173 could be due to other types of Fe-silicides and Fe atoms diluted in the matrix. With half-  
 174 metallic band structure, hexagonal Fe<sub>2</sub>Si phase is ferromagnetic and the magnetic moment is  
 175 about 1.30 μB/Fe [40-42]. For ferromagnetic Fe<sub>5</sub>Si<sub>3</sub> phase, it has two unequal sites, with  
 176 magnetic moments of 1.05 μB/Fe and 1.55 μB/Fe [40], respectively. Thus, the average  
 177 magnetic moment of Fe<sub>5</sub>Si<sub>3</sub> is 1.30 μB/Fe. The magnetic moment values for other Fe-silicides  
 178 can be referred to the literature [40, 41, 43].

179 *Fig. 4*

180 Fig. 4(c)-(d) show the M-H curves at 10 K and 300 K. In Fig. 4(c), the hysteretic behavior  
 181 is clear at low fields and the saturation magnetization is about 1.40 μB/Fe at 10 K. In contrast,  
 182 no hysteretic behavior was observed in Fig. 4(d) at low fields at 300 K. This demonstrates the  
 183 ferromagnetic behavior at 10 K and the superparamagnetic behavior at 300 K.

184 Then, we discuss the ferromagnetism at 10 K. 4H-SiC matrix is diamagnetic and the  
 185 implanted Fe atoms induce the ferromagnetic behavior. The ferromagnetism is an  
 186 accumulation of total Fe atoms, as expressed below:

$$187 \quad \langle M \rangle = \sum_{i=1}^n f_i \langle M \rangle_i$$

188 where  $\langle M \rangle$  is the saturation magnetization, about 1.40 μB/Fe at 10 K,  $f_i$  and  $\langle M \rangle_i$  are the Fe  
 189 fraction and the magnetic moment in each component. Taking into account the presence of

190 Fe-rich nanoparticles, Fe in 4H-SiC matrix contains two parts: Fe atoms in matrix and inside  
 191 Fe-silicides. Thus, the above equation can be written as:

$$192 \quad \langle M \rangle = f_{diluted} \langle M \rangle_{diluted} + f_{nano} \langle M \rangle_{nano}$$

193 where  $\langle M \rangle_{diluted}$  and  $\langle M \rangle_{nano}$  represent the average magnetic moments for the Fe atoms in  
 194 matrix and inside nanoparticles, respectively, and  $f_{diluted}$  and  $f_{nano}$  are the Fe fractions in  
 195 matrix and inside nanoparticles. The Fe distribution is extracted from APT analyses and the  
 196 results are listed in Table 1.

197 **Table 1 Fe distribution and the magnetic contributions**

	Nanoparticles					
	Matrix	Fe <sub>2</sub> Si	Fe <sub>5</sub> Si <sub>3</sub>	Fe <sub>3</sub> Si <sub>2</sub>	FeSi	FeSi <sub>2</sub>
$f_i / \%$	48.3	34.6	6.1	8.0	2.6	0.4
$\langle M_i \rangle / \mu\text{B}/\text{Fe}$	1.59	1.3 [40-42]	1.3 [40]	0.79 [43]	0.75 [43]	0 [43]
$\langle M \rangle_{nano} / \mu\text{B}/\text{Fe}$	1.18					

198 **Note:**  $\langle M \rangle_{nano}$  represents the average magnetic moment for the Fe atoms inside nanoparticles.

199 From APT analyses, about 51.7% of total Fe atoms form Fe-silicides. The average magnetic  
 200 moment of nanoparticles is about 1.18  $\mu\text{B}/\text{Fe}$ , while that for diluted Fe atoms is about 1.59  
 201  $\mu\text{B}/\text{Fe}$ . The magnetic moment for the diluted Fe atoms is close to that for 6 at.% Fe implanted  
 202 6H-SiC, with a value of 1.65  $\mu\text{B}/\text{Fe}$  [44]. Fe<sub>2</sub>Si phase, with a Fe fraction of 34.6%, is the main  
 203 contributor among all the Fe-silicides. The half-metallic ferromagnetism of Fe<sub>2</sub>Si is mainly  
 204 due to the Fe *d-d* exchange as well as the hybridization between Si *p* and Fe *d* orbitals [45].  
 205 Compared with 6 at.% Fe, a 2 at.% Fe implantation induces a larger variety of Fe-silicides,  
 206 while, in both cases, not only the diluted Fe atoms but the Fe atoms inside nanoparticles are  
 207 also important to the ferromagnetism. According to *ab initio* calculations, the ferromagnetic  
 208 ordering within the diluted Fe atoms derives from the Si substitution by Fe in the (Si/4C)

209 tetrahedron, in which the electronic structure of Fe atoms is strongly affected by the  
210 neighboring C atoms [46]. An increase of the Fe-C length along the *c* direction of this (Fe/4C)  
211 tetrahedron leads to the increased mean magnetic moment [46]. Calculated densities of states  
212 on Si substitution with Fe reveal the Fe bands in the gap close to the SiC valence band top, in  
213 which a significant degree of coupling exists between Fe 3*d* and C 2*p* orbitals [46, 47].

214 To conclude, this work concentrates on a 2 at.% Fe-implanted 4H-SiC DMS. Combined  
215 high resolution APT and STEM analyses reveal a chain of magnetic Fe-silicides, including  
216 Fe<sub>3</sub>Si, Fe<sub>2</sub>Si, Fe<sub>5</sub>Si<sub>3</sub>, Fe<sub>3</sub>Si<sub>2</sub>, FeSi and FeSi<sub>2</sub>, which display both size and composition gradient  
217 characteristics along the implantation depth. Fe<sub>2</sub>Si phase possesses larger proportion than any  
218 other type. The DMS exhibits a ferromagnetic behavior at 10 K and the ferromagnetism  
219 originates from both the diluted Fe atoms and Fe-silicides. The average magnetic moment of  
220 nanoparticles was estimated to be about 1.18 μB/Fe, while that for diluted Fe atoms is about  
221 1.59 μB/Fe at 10 K.

## 222 **Declaration of Competing Interest**

223 The authors declare that they have no known competing financial interests or personal  
224 relationships that could have appeared to influence the work reported in this paper.

## 225 **Acknowledgements**

226 This work belongs to the MAGMA project, funded by Région Normandie and the European  
227 Regional Development Fund of Normandy (ERDF).

## 228 **References:**

229 [1] Dietl T, Ohno H, Matsukura F, Cibert J, Ferrand ED. *Science* 2000;287:1019.

230 [2] Dietl T, Ohno H. *Rev Mod Phys* 2014;86:187.

231 [3] Dietl T, Sato K, Fukushima T, Bonanni A, Jamet M, Barski A, Kuroda S, Tanaka M, Hai PN. *Rev Mod*

- 232 *Phys* 2015;87:1311.
- 233 [4] Jungwirth T, Wang KY, Mašek J, Edmonds KW, König J, Sinova J, Polini M, Goncharuk NA,  
234 MacDonald AH, Sawicki M. *Phys Rev B* 2005;72:165204.
- 235 [5] Ohno H, Shen A, Matsukura F, Oiwa A, Endo A, Katsumoto S, Iye Y. *Appl Phys Lett* 1996;69:363.
- 236 [6] Biswas K, Sardar K, Rao C. *Appl Phys Lett* 2006;89:132503.
- 237 [7] Harris CI, Savage S, Konstantinov A, Bakowski M, Ericsson P. *Appl Surf Sci* 2001;184:393.
- 238 [8] Shaposhnikov VL, Sobolev NA. *J Phys Condens Matter* 2004;16:1761.
- 239 [9] Theodoropoulou N, Hebard AF, Chu S, Overberg ME, Abernathy CR, Pearton SJ, Wilson RG, Zavada  
240 JM, Park YD. *J Vac Sci Technol A* 2002;20:579.
- 241 [10] Diallo L, Fnidiki A, Lechevallier L, Zarefy A, Juraszek J, Cuvilly F, Blum I, Viret M, Marteau M, Eyidi  
242 D. *IEEE Magn Lett* 2018;9:1.
- 243 [11] Diallo ML, Lechevallier L, Fnidiki A, Lardé R, Debelle A, Thomé L, Viret M, Marteau M, Eyidi D,  
244 Declémy A. *J Appl Phys* 2015;117:183907.
- 245 [12] Song B, Bao H, Li H, Lei M, Peng T, Jian J, Liu J, Wang W, Wang W, Chen X. *J Am Chem Soc*  
246 2009;131:1376.
- 247 [13] Song B, Jian JK, Li H, Lei M, Bao HQ, Chen XL, Wang G. *Physica B* 2008;403:2897.
- 248 [14] Song B, Chen XL, Han JC, Jian JK, Bao HQ, Li H, Zhu KX, Wang WY, Wang G, Zuo HB. *J Phys D*  
249 *Appl Phys* 2010;43:415002.
- 250 [15] Liu Y, Wang G, Wang S, Yang J, Chen L, Qin X, Song B, Wang B, Chen X. *Phys Rev Lett*  
251 2011;106:87205.
- 252 [16] Li L, Prucnal S, Yao SD, Potzger K, Anwand W, Wagner A, Zhou S. *Appl Phys Lett* 2011;98:222508.
- 253 [17] Al Azri M, Elzain M, Bouziane K, Chérif SM, Roussigné Y, Declémy A, Drouet M, Thomé L. *J Appl Phys*  
254 2012;111:07C315.
- 255 [18] Shinya H, Fukushima T, Masago A, Sato K, Katayama-Yoshida H. *Phys Rev B* 2017;96:104415.
- 256 [19] Kuryliszyn Kudelska I, Diduszko R, Tymicki E, Dobrowolski W, Graszka K. *Phys Status Solidi (b)*  
257 2007;244:1743.
- 258 [20] Inoue A, Furukawa S, Masumoto T. *Metall Mater Trans A* 1987;18:715.
- 259 [21] Declémy A, Dupeyrat C, Thomé L, Debelle A. *Mater Sci Forum* 2009;615:461.
- 260 [22] Dupeyrat C, Declémy A, Drouet M, Eyidi D, Thomé L, Debelle A, Viret M, Ott F. *Physica B*  
261 2009;404:4731.

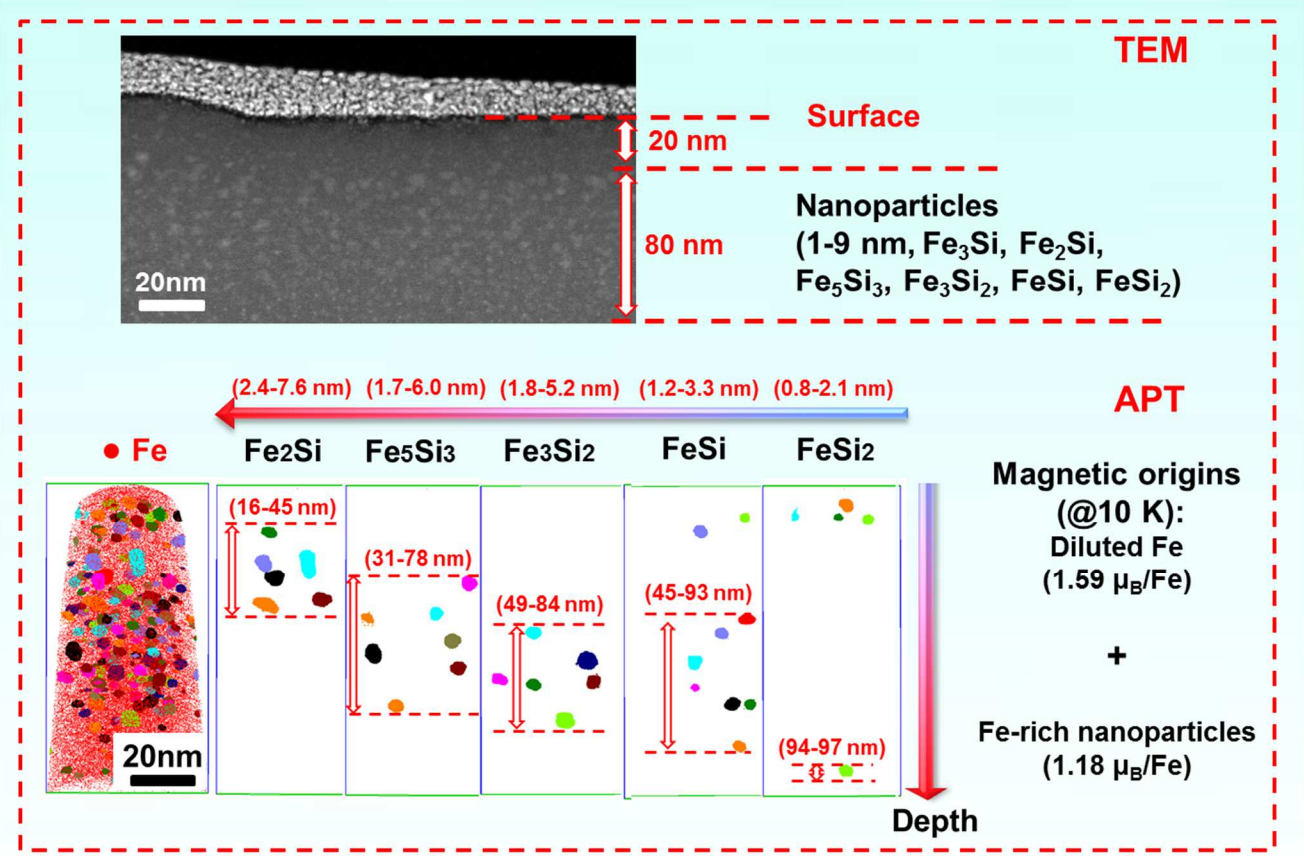
- 262 [23] Declémy A, Debelle A, Dupeyrat C, Thomé L, Monnet I, Eyidi D. *Appl Phys A* 2012;106:679.
- 263 [24] Lefevre J. PhD thesis, *École Polytechnique*, 2008.
- 264 [25] Lefebvre W, Vurpillot F, Sauvage X. *Academic Press*. 2016.
- 265 [26] Momma K, Izumi F. *J Appl Crystallogr* 2011;44:1272.
- 266 [27] Fnidiki A, Richomme F, Teillet J, Pierre F, Boher P, Houdy P. *J Magn Magn Mater* 1993;121:520.
- 267 [28] Eymery JP, Fnidiki A, Riviere JP. *Nucl Instrum Meth Phys Res* 1983;209:919.
- 268 [29] Juraszek J, Zivotsky O, Chiron H, Vaudolon C, Teillet J. *Rev Sci Instrum* 2009;80:43905.
- 269 [30] Gunnlaugsson HP, Bharuth-Ram K, Dietrich M, Fanciulli M, Fynbo HOU, Weyer G. *Hyperfine Interact*  
270 2006;169:1319.
- 271 [31] Thuvander M, Weidow J, Angseryd J, Falk LK, Liu F, Sonestedt M, Stiller K, André H.  
272 *Ultramicroscopy* 2011;111:604.
- 273 [32] Peng Z, Vurpillot F, Choi P, Li Y, Raabe D, Gault B. *Ultramicroscopy* 2018;189:54.
- 274 [33] Hatzoglou C, Radiguet B, Vurpillot F, Pareige P. *J Nucl Mater* 2018;505:240.
- 275 [34] Lacaze J, Sundman B. *Metall Trans A* 1991;22:2211.
- 276 [35] Tang WM, Zheng ZX, Ding HF, Jin ZH. *Mater Chem Phys* 2002;74:258.
- 277 [36] Bouziane K, Al Azri M, Elzain M, Chérif SM, Mamor M, Declémy A, Thomé L. *J Alloy Compd*  
278 2015;632:760.
- 279 [37] Kuryliszyn Kudelska I, Diduszko R, Tymicki E, Dobrowolski W, Graszka K. *Phys Status Solidi (b)*  
280 2007;244:1743.
- 281 [38] Vinzelberg H, Schumann J, Elefant D, Arushanov E, Schmidt OG. *J Appl Phys* 2008;104:93707.
- 282 [39] Lin F, Jiang D, Ma X, Shi W. *Thin Solid Films* 2007;515:5353.
- 283 [40] Johnson V, Weiher JF, Frederick CG, Rogers DB. *J Solid State Chem* 1972;4:311.
- 284 [41] Shinjo T, Nakamura Y, Shikazono N. *J Phys Soc Jpn* 1963;18:797.
- 285 [42] Tang CP, Tam KV, Xiong SJ, Cao J, Zhang X. *AIP Adv* 2016;6:65317.
- 286 [43] Yang Z, Wu S, Zhao X, Nguyen MC, Yu S, Wen T, Tang L, Li F, Ho K, Wang C. *J Appl Phys*  
287 2018;124:73901.
- 288 [44] Diallo ML. PhD thesis, *Université de Rouen Normandie*, 2017.
- 289 [45] Chen W, Li R, Liu Y. *Adv Mater Sci Eng*, 2017.
- 290 [46] Los AV, Timoshevskii AN, Los VF, Kalkuta SA. *Phys Rev B* 2007;76:165204.
- 291 [47] Sato K, Bergqvist L, Kudrnovský J, Dederichs PH, Eriksson O, Turek I, Sanyal B, Bouzerar G,

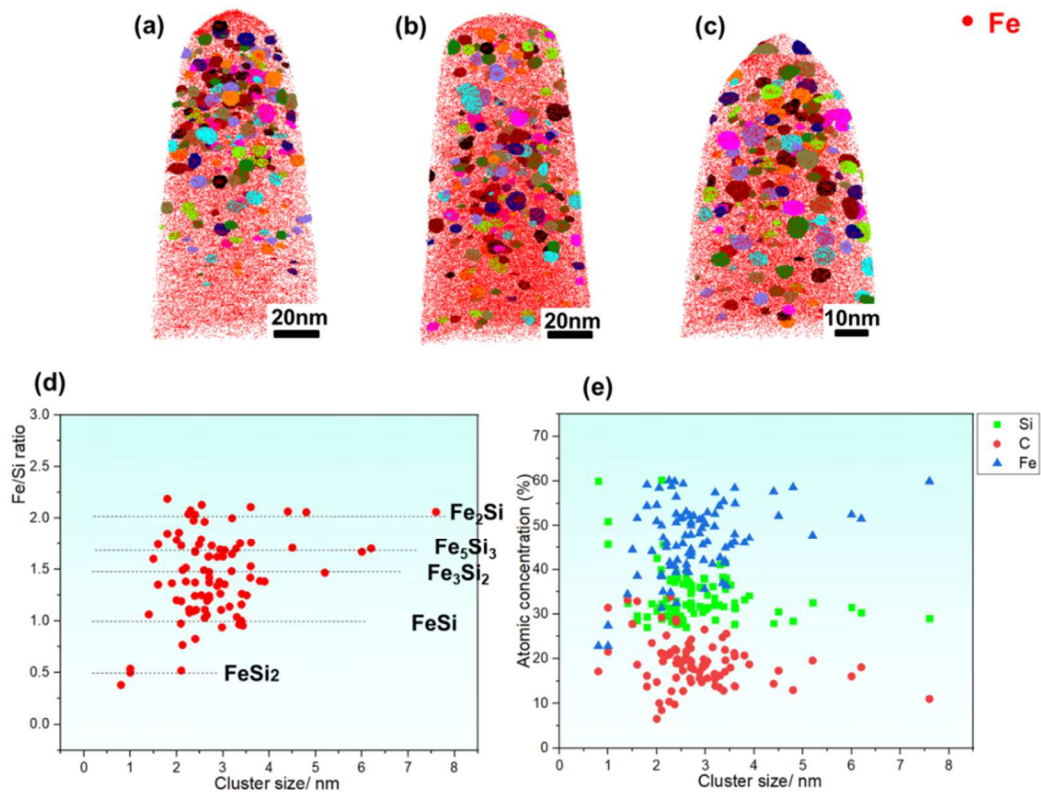
292

*Katayama-Yoshida H, Dinh VA. Rev Mod Phys 2010;82:1633.*

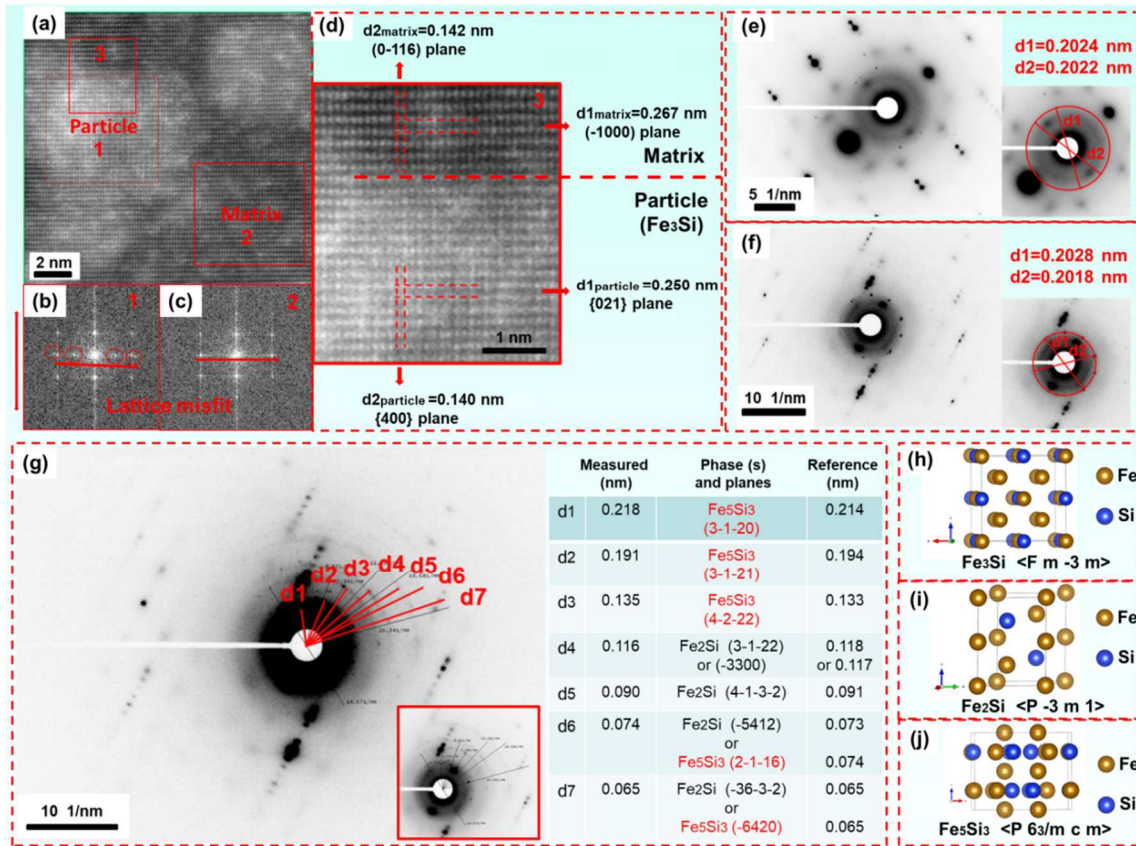
293

# Graphical abstract

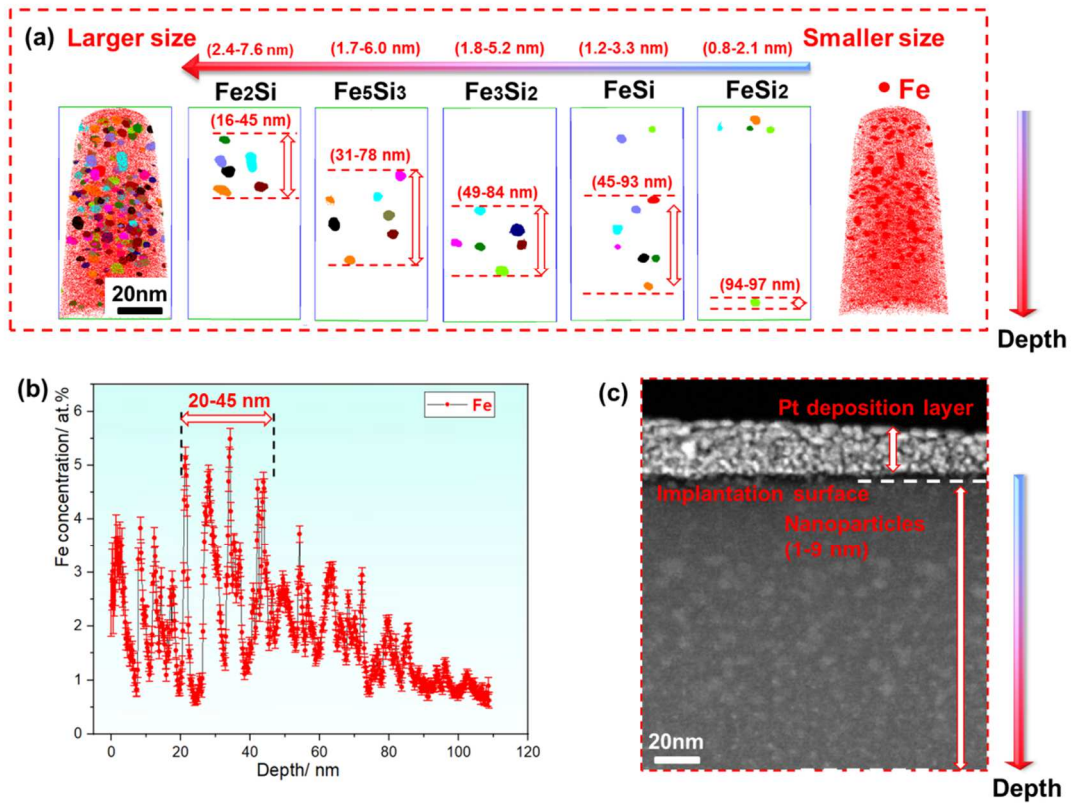




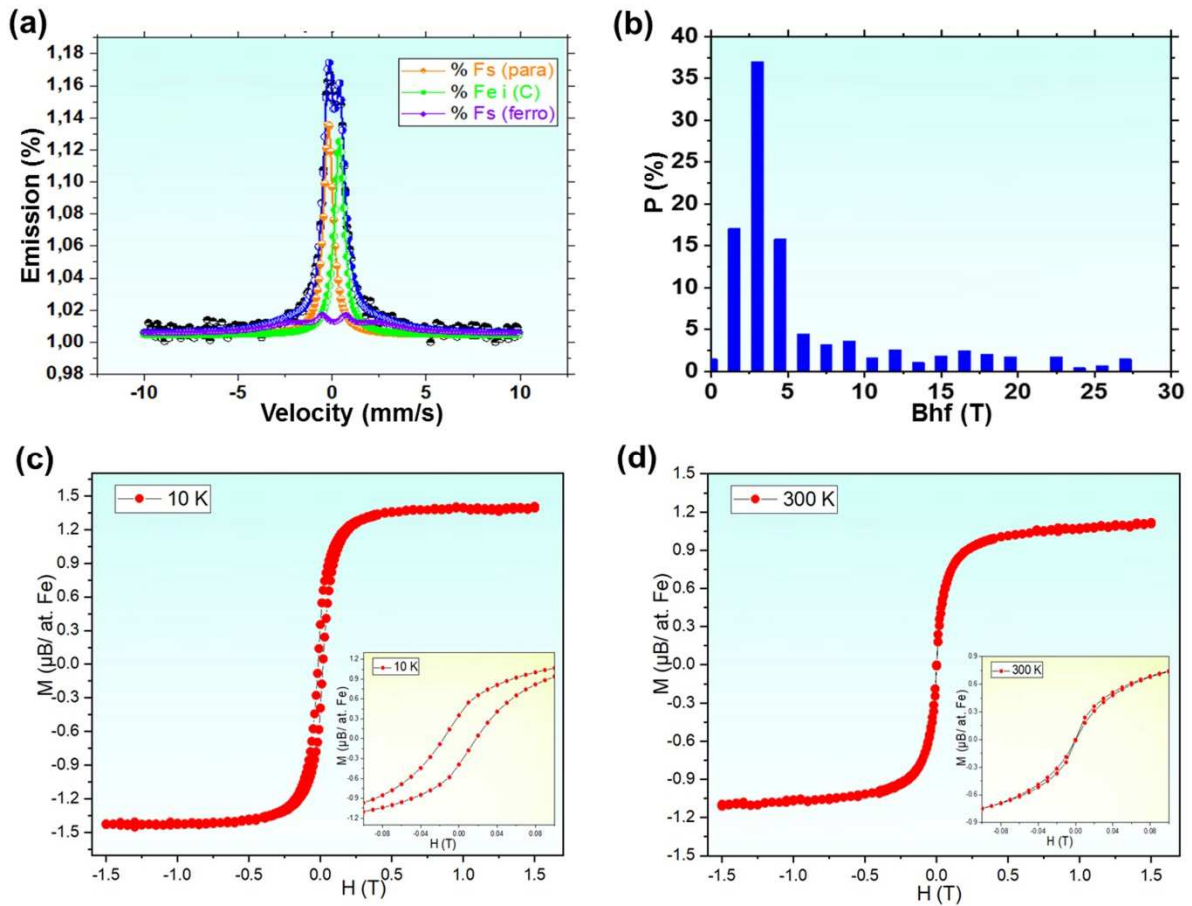
*Fig. 1 Distribution map of Fe atoms and nanoparticles in 2 at.% Fe-implanted 4H-SiC after annealing at 1300 °C for 4 min: (a)-(c) three reconstructed APT tips with the identified nanoparticles; (d) the calculated Fe/Si ratio from the core nanoparticles (for those with 60 atoms in minimum); (e) the calculated atomic concentrations of the core nanoparticles (for those with 60 atoms in minimum). In (d), the dashed lines correspond to different types of Fe-silicides.*



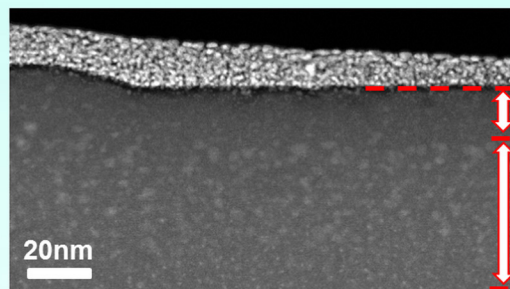
**Fig. 2** STEM/HRTEM analyses of crystal structures for  $Fe_3Si$ ,  $Fe_2Si$  and  $Fe_5Si_3$  phases: (a) HRTEM image revealing cubic  $Fe_3Si$  phase; (b)-(c) the FFT images of the nanoparticle (as marked with “1”) and the matrix (as marked with “2”); (d) the local magnification image displaying the matrix-nanoparticle interface (as marked with “3”); (e)-(f) the SAEDP images showing hexagonal  $Fe_2Si$  phase; (g) the SAEDP image (as well as the inserted one with distinct contrast) with the corresponding interplanar distances revealing the hexagonal  $Fe_5Si_3$  phase; (h)-(j) the repeated lattice cells of  $Fe_3Si$ ,  $Fe_2Si$  and  $Fe_5Si_3$  phases from VESTA software, respectively.



*Fig. 3 Distribution map of the nanoparticles from APT and TEM analyses: (a) reconstructed APT tip revealing the gradient distribution of a chain of Fe-silicides (including  $\text{Fe}_2\text{Si}$ ,  $\text{Fe}_5\text{Si}_3$ ,  $\text{Fe}_3\text{Si}_2$ ,  $\text{FeSi}$  and  $\text{FeSi}_2$ ); (b) Fe distribution along the irradiation depth; (c) the nanoparticles formed beneath the implantation surface.*



**Fig. 4** Photographs exhibiting the room-temperature CEMS spectra (a) with the corresponding hyperfine field distribution (b) and the magnetization hysteresis curves measured at 10 K (c) & 300 K (d) for the samples annealed at 1300 °C for 4 min. In (a), the whole spectrum (in blue) and 3 components consisting of the Fe<sub>i</sub> (C) component (in green), the Fs (para) component (in orange) and the Fs (ferro) component (in purple) are displayed. In (c) & (d), the inserted photos show the magnetization behaviors at low fields.

**TEM****Surface**

20 nm

**Nanoparticles**(1-9 nm,  $\text{Fe}_3\text{Si}$ ,  $\text{Fe}_2\text{Si}$ ,  
 $\text{Fe}_5\text{Si}_3$ ,  $\text{Fe}_3\text{Si}_2$ ,  $\text{FeSi}$ ,  $\text{FeSi}_2$ )

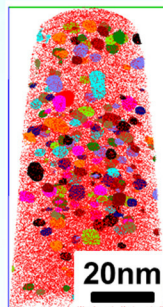
80 nm

20nm

**APT**

(2.4-7.6 nm) (1.7-6.0 nm) (1.8-5.2 nm) (1.2-3.3 nm) (0.8-2.1 nm)

● Fe

 $\text{Fe}_2\text{Si}$  $\text{Fe}_5\text{Si}_3$  $\text{Fe}_3\text{Si}_2$  $\text{FeSi}$  $\text{FeSi}_2$ 

(16-45 nm)

(31-78 nm)

(49-84 nm)

(45-93 nm)

(94-97 nm)

**Magnetic origins**(@10 K):  
Diluted Fe  
( $1.59 \mu_B/\text{Fe}$ )

+

**Fe-rich nanoparticles**  
( $1.18 \mu_B/\text{Fe}$ )**Depth**